Error and Uncertainty Degrade Topographic Corrections of Remotely Sensed Data

Jeff Dozier[1], Edward H. Bair[2], Latha Baskaran[3], Philip G. Brodrick[3], Nimrod Carmon[3], Raymond F. Kokaly[4], Charles E. Miller[3], Kimberley R. Miner[3], Thomas H. Painter[5], and David R. Thompson[3]

[1]Bren School of Environmental Science & Management, University of California, Santa Barbara, CA 93106. [2]Earth Research Institute, University of California, Santa Barbara, CA 93106. [3]Jet Propulsion Laboratory, California Institute of Technology, Pasadena, CA 91109. [4]U.S. Geological Survey, Lakewood, CO 80225. [5]Joint Institute for Regional Earth System Science and Engineering, University of California, Los Angeles, CA 90095.

Corresponding author: Jeff Dozier (dozier@ucsb.edu)

Key Points:

- Mountain topography causes apparent remotely sensed reflectance to differ from the intrinsic reflectance of the surface.
- Errors in solar geometry derived from globally available digital elevation models introduce substantial uncertainty into analyses.
- Retrieval of the intrinsic reflectance and surface biogeophysical properties requires assessment of and correction for topographic effects.

Abstract

Chemical and biological composition of surface materials and physical structure and arrangement of those materials determine the *intrinsic* reflectance of Earth's land surface. the *apparent* reflectance—as measured a spaceborne or airborne sensor that has been corrected for atmospheric attenuation—depends also on topography, surface roughness, and the atmosphere. Especially in Earth's mountains, estimating properties of scientific interest from remotely sensed data requires compensation for topography. Doing so requires information from digital elevation models (DEMs). Available DEMs with global coverage are derived from spaceborne interferometric radar and stereo-photogrammetry at ~30 m spatial resolution. Locally or regionally, lidar altimetry, interferometric radar, or stereo-photogrammetry produces DEMs with finer resolutions. Characterization of their quality typically expresses the root-mean-square (RMS) error of the elevation, but the accuracy of remotely sensed retrievals is sensitive to uncertainties in topographic properties that affect incoming and reflected radiation and that are inadequately represented by the RMS error of the elevation. The most essential variables are the cosine of the local solar illumination angle on a slope, the shadows cast by neighboring terrain, and the view factor, the fraction of the overlying hemisphere open to the sky. Comparison of global DEMs with locally available fine-scale DEMs shows that calculations with the global products consistently underestimate the cosine of the solar angle and underrepresent shadows. Analyzing imagery of Earth's mountains from current and future spaceborne missions requires addressing the uncertainty introduced by errors in DEMs on algorithms that analyze remotely sensed data to produce information about Earth's surface.

Plain Language Summary

Earth's mountain regions significantly influence the planet's climate, hydrology, ecology, and geology. Studying them with remote sensing requires that we compensate for the influence of topography on the reflection of solar radiation. Digital Elevation Models (DEMs) are used across scientific disciplines to understand topography's effect on the remotely sensed signal. Small errors in the estimates of elevation lead to larger errors in calculations of the solar illumination on the terrain and portions that are in shadow, thereby leading to misinterpretation of remotely sensed imagery from satellites and airplanes. Here, we present estimates of the errors and uncertainty in DEM retrievals, and we identify some outright mistakes. Compensating for uncertainty will inform algorithms that consider the effect of Earth's topography, improving the characterization from satellite missions of attributes of the planet's surface.

1 Introduction

We use remotely sensed data to derive geophysical and biological properties of importance to the study of Earth and other planets. On Earth these analyses must include mountains, which play a key role in the planet's climate, hydrology, ecology, and geology.

For example, mountains drive orographic enhancement of precipitation and lead to their function as the world's water towers, resources at risk in a warming climate (Immerzeel et al., 2020; Viviroli et al., 2007). About a quarter of Earth's land surface is

mountainous (Wrzesien et al., 2019, 12% to 39% depending on the definition of "mountainous"), but mountain snowmelt supplies water resources for more than one billion people (Mankin et al., 2015), serving an important water storage role as climate warming transitions some snow to rain (Barros, 2013). Further, vegetation changes in high mountains indicate carbon-dioxide fertilization in areas where the partial pressure of all gases is lower (Shugart et al., 2001). Combinations of drought and fire affect mountain forests and sources of water (Moody & Martin, 2001). The critical role that mountains serve as water towers and vegetation hotspots may change under climate change, contributing to hazards to people living in or relying on mountain resources (Kirschbaum et al., 2020).

The recent National Academies' Decadal Survey for Earth science and applications, *Thriving on our Changing Planet,* reflects these multiple concerns, with recommendations calling for observations "at scales driven by topographic variability" to reflect the heterogeneity of ecological, hydrological, and geological dynamics in Earth's mountains (National Academies of Sciences, Engineering, & Medicine, 2018). Investigating these processes via remote sensing requires spatial resolutions fine enough to characterize the variability, recognizing that the topography affects the reflected signals, thereby affecting the retrieval algorithms that interpret the state variables and fluxes of energy and mass.

Analysis of the topographic effect requires information in digital elevation models of the bare surface, usually but not universally meaning DEMs, as distinct from digital surface models (DSMs) that include vegetation, buildings, or other features. We consider two globally available DEM datasets: the NASADEM (Buckley, 2020) and the Copernicus DEM (European Space Agency, 2021), both distributed at a resolution of 1 arcsecond (~30 m at the Equator). Locally or regionally, finer-resolution DEMs are available, so we consider three of those, which were derived by lidar, interferometric synthetic aperture radar, and structure-from-motion stereo photogrammetry from fine-resolution images. Our analysis considers the fine-resolution DEMs, in three different terrains, to provide the best assessment of the topographic effects on solar illumination geometry, and we compare those assessments to those derived from the two globally available datasets.

Characterization of the quality of DEMs typically assesses the vertical accuracy of the elevation. Uuemaa et al. (2020), through comparison of globally available products with fine-resolution lidar elevations, estimated root-mean-square (RMS) errors of 8-10 m for the NASADEM and TanDEM-X datasets (TanDEM-X is the primary source of data for the Copernicus DEM). Guth and Geoffroy (2021) compared several datasets with airborne lidar and ICESat-2 data and preferred the Copernicus DEM based on its ability to penetrate vegetation canopies and retrieve bare-Earth elevations.

However, the focus on elevation errors misses the effect of the topography on remotely sensed information in the wavelengths of the solar spectrum, which lies with the solar illumination geometry. The cosine of the local solar angle and the shadows cast by neighboring terrain are the most important variables for remote sensing of Earth's surface in the reflective domain. On clear days, most of the irradiance is direct, but the diffuse component is significant (~30%) at the blue end of the solar spectrum. The surrounding landscape causes multiple reflections, which can be represented by the sky view factor—

the fraction of the overlying hemisphere open to the sky. The topographic variables that affect the solar angles also affect the viewing angles from the sensor.

We therefore assess the DEMs based on their ability to provide insight into the ways that topography affects our ability to retrieve properties of the surface important to the study of Earth science. Fundamentally, retrievals that are sensitive to the magnitude of the spectral reflectance will be most affected. Examples include snow albedo (Bair et al., 2021; Painter et al., 2013) and ecosystem composition (Bogan et al., 2019). Retrievals that utilize the shape of the reflectance spectrum, characterized for example by the spectral angle (Kruse et al., 1993), will be less affected but not entirely immune because the fraction of the incident irradiance that is diffuse vs. direct is sensitive to the topography. Finally, retrievals that depend on the wavelength of absorption features do not depend on the magnitude of the reflectance. The primary example is mineral identification in soils and vegetation, which requires enough illumination to identify spectral features (Clark et al., 2003; Mulder et al., 2013).

2 Data and Methods

2.1 Acronyms

ASO	Airborne Snow Observatories
ASTER	Advanced Spaceborne Thermal Emission and Reflection Radiometer
AVIRIS-NG	Airborne Visible and Infrared Imaging Spectrometer – Next Generation
CHIME	Copernicus Hyperspectral Imaging Mission for the Environment
DEM	Digital elevation model of the bare Earth surface
DSM	Digital surface model including vegetation, buildings, etc.
DTM	Same as DEM
EMIT	Earth Surface Mineral Dust Source Investigation
EnMAP	Environmental Mapping and Analysis Program
EROS	Earth Resources Observation and Science
HMA	High Mountain Asia
IFSAR	Interferometric synthetic aperture radar
InSAR	Same as IFSAR
ISRO	Indian Space Research Organization
NASA	National Aeronautics and Space Administration
NOAA	National Oceanic and Atmospheric Administration
OLI	Operational Land Imager
SBG	Surface Biology and Geology mission
SRTM	Shuttle Radar Topography Mission
USGS	US Geological Survey
UTC	Coordinated Universal Time
Ellipsoids and Geoids	
EGM2008	Earth Gravitational Model 2008
EGM96	Earth Gravitational Model 1996
GRS80	Geodetic Reference System 1980
NAD83	North American Datum of 1983

NAVD88	North American Vertical Datum of 1988
WGS84	World Geodetic System 1984

2.2 Elevation data

We consider two spatial resolutions of digital elevation models: fine and coarse. The coarse-resolution datasets are available globally, whereas the fine-resolution data are available selectively in specific locations. Table 1 summarizes the information sources for three fine-resolution and two global coarse-resolution datasets.

Insert Table 1 near here

For the fine-resolution imagery, data are derived from three different methods: lidar altimetry, interferometric synthetic aperture radar, and structure-from-motion using fine-resolution commercial satellite imagery.

1. Airborne Snow Observatories Inc. (Painter et al., 2016) maps snow depth with lidar altimetry over drainage basins in the Western U.S., Switzerland, and Norway. The operation acquires elevation data during the snow-free summer and then periodically measures the snow-on elevation during the winter and derives snow depth by subtraction. The company provided a 3 m DEM of the Carson River Watershed in the Sierra Nevada of California/Nevada, covering 2052 km^2.
2. The U.S. Geological Survey's Alaska Mapping Initiative acquired airborne interferometric synthetic aperture radar (InSAR) data over much of Alaska in 2010 and 2012 (USGS EROS Archive, 2018). InSAR acquisitions can take place even in cloudy weather, and the data from a high latitude provide a broad range of solar illumination angles during the year. We downloaded and spliced tiles at 5 m resolution for a 2582 km^2 area in the Wrangell Mountains in Southeast Alaska.
3. Shean et al. (2016) employ structure-from-motion to measure elevation using commercial fine-resolution satellite imagery. From the National Snow and Ice Data Center, we downloaded part of the High Mountain Asia 8 m DEM for a 3514 km^2 area in the Himachal Pradesh state in the Indian Himalaya that covers 9 flight lines of the 2016 NASA-ISRO AVIRIS-NG campaign (Space Applications Centre, 2017).

For the coarse resolution imagery, we used two global data sources at one arcsecond resolution distributed in geographic (latitude-longitude) format. In cropping to the boundaries of each fine-resolution area, we added 5 km to each edge to minimize edge effects in calculating topographic parameters.

1. We spliced 1° × 1° tiles from the NASADEM (Buckley, 2020) together because our areas of interest crossed latitude or longitude tile boundaries. The NASADEM combines information from the Shuttle Radar Topography Mission (Farr et al., 2007) and stereo-photogrammetry from ASTER imagery (NASA & METI, 2019).
2. We downloaded Copernicus DEMs (European Space Agency, 2021) that were spliced and distributed by Open Topography. The Copernicus DEM is derived from TanDEM-X imagery.

Figure 1 shows the Copernicus DEM on the left and the ASO DEM on the right for the Carson River Watershed. The red rectangle in the left-hand image shows the area that the ASO DEM illustrates the detail of the topographic data at 3 m spatial resolution.

Insert Figure 1 near here

2.3 Notation

We selected or calculated the following variables for each grid point in each elevation dataset. $\theta_0, \phi_0, \mu_S, F_{dif}$, and I vary with date; the other variables are independent of date and thus the solar illumination. Deep snow can smooth the topography, but our comparisons of snow-off with snow-on elevations find only a few grid cells with significantly different slope and azimuth. At the 3 m spatial resolution of the Carson River DEM, the RMS difference in slopes between the snow-on and snow-off elevations is 1.8°, and the 99th percentile absolute difference is 6.8°. Resampled to 10 m spatial resolution, the RMS difference is 1.3°, and the 99th percentile absolute difference is 5.3°.

θ_0, ϕ_0	Solar zenith and azimuth angles, $\mu_0 = \cos\theta_0$
μ_S	Cosine of solar illumination angle on a slope, set to zero for slopes that are in shadow, either by adjacent terrain or when μ_S is negative
ρ	Spectral directional-hemispherical or bihemispherical reflectance, depending on subscripts (Schaepman-Strub et al., 2006)
F_{dif}	Fraction of incoming spectral irradiance that is diffuse
H_ϕ	Angle to the topographic horizon, upward from horizontal, in azimuth direction ϕ
I	Spectral irradiance, incoming or reflected depending on subscript
RMS	Root-mean-square value $RMS(x) = \sqrt{\frac{1}{N}\sum_{n=1}^{N}\lvert x_n\rvert^2}$
S, A	Slope angle, upward from horizontal, and slope azimuth, south at 0°, eastward positive and westward negative, consistent with a right-hand coordinate system
V_Ω	Sky view factor, hereafter just view factor, the fraction of the upward hemisphere open to the sky
Z	Elevation of the surface

2.4 Methods

We compared topographic variables by reprojecting both fine- and coarse-resolution data to an intermediate resolution approximating the geometric mean of the two resolutions, thereby to include the range and distribution of topographic values in the landscape. The one-arcsecond resolution of the NASADEM and Copernicus DEM translate to about 30 m. For the Carson River Watershed, the intermediate resolution between the 3 m ASO lidar and the globally available data is 10 m. For the InSAR data at 5 m over the Wrangell Mountains in Alaska, the intermediate resolution is 12 m. For the 8 m data in the HMA DEM, the intermediate resolution is 15 m. We assume the fine DEM is more accurate, particularly because variables derived over multiple points are compared to those derived from an individual location in the coarse DEM; therefore, the RMS of the difference between the coarse and fine estimates of a variable is considered the RMS error in the coarse-resolution data.

Insert Figure 2 near here

We calculated μ_S for seven dates between the winter and summer solstices, spaced so that the intervals between the solar declinations were equal (Figure 2). For every date, we chose 10:45 in the local time zone to match typical mid-morning acquisition times of satellites: Pacific Standard (UTC–8:00) for the Carson River, Alaska Standard (UTC–9:00) for the Wrangell Mountains, and India Standard (UTC+5:30) for the Himachal Pradesh. Figure 3 shows cosine of solar illumination angles for the Himachal Pradesh on the seven dates in Figure 2. The pixels are more illuminated as the solar illumination angle gets closer to zenith, and the fraction of diffuse illumination decreases, thereby affecting the relationship between intrinsic and apparent reflectance .

Insert Figure 3 near here

3 An Illustration of the Problem

Insert Figure 4 near here

Figure 4 shows two images and two graphs. The upper left (Figure 4a) shows band 5 (center wavelength 865 nm) of a Landsat 8 OLI image of the Indian Himalaya, acquired on 22 February 2016 over the Himachal Pradesh state of India. We chose band 5 because of the small fraction of diffuse illumination in the solar spectrum in those wavelengths. Figure 4b shows a calculation of μ_S, the cosine of the solar illumination angle at the same date and time as the Landsat image, using elevation data from NASADEM (Buckley, 2020). The cosines are calculated from the slope and aspect of the terrain and the solar zenith and azimuth angles on a flat surface. Where shaded by local horizons or by the slope itself, the cosines are set to zero. Superficially, the two images appear to match, allowing that some illuminated areas are dark because that surface material is dark, whereas shadows are dark even if the surface material is bright. The bright areas in the Landsat image correspond to highly illuminated pixels. However, the scatter density plot (Figure 4c) indicates some problematic values. The high reflectance values in the upper left corner of Figure 4c correspond to pixels either in shadow or with highly oblique solar illumination, indicating that the solar angle calculated from the DEM is wrong. The low reflectance values in the lower right corner of the scatter plot tell a similar but more ambiguous story. These dark pixels are well illuminated; they could represent a dark surface, or they might not truly be well illuminated. Figure 4d shows probability density functions (pdf) of the reflectance values in areas of low ($\mu_S < 0.2$) and high ($\mu_S > 0.87$) illumination (each threshold represents 14% of the image). Each pdf has a long tail. Those in the tail of the low illumination category indicate that μ_S is not correctly estimated and is too small. With a correct DEM, we would not see such high reflectance values at highly oblique solar illumination, because of the low values of incident irradiance at those locations.

Algorithms that retrieve land surface properties analyze the spectral "reflectance," broadly defined to cover the several possible angular reflectance configurations that Schaepman-Strub et al. (2006) articulate. In their study of the effects of surface roughness on snow albedo, Bair et al. (2022) defined *intrinsic* reflectance of a substance independent of effects of roughness or topography. The corresponding *apparent* value, as one might measure at a plot, incorporates artifacts caused by roughness or topography. For example, the intrinsic reflectance of clean snow in the visible wavelengths cannot drop to 0.2, but the apparent reflectance of shadowed snow can reach such low values. Corrected for

atmospheric effects, measurements of spectral top-of-atmosphere radiance by a satellite sensor can be converted to apparent values of, for example, bihemispherical reflectance or bidirectional reflectance (Schaepman-Strub et al., 2006). Retrieval of a parameter of interest at Earth's surface using these data requires an estimate of the intrinsic spectral reflectance, interpreted by a combination of topographic information and the apparent value derived from the satellite sensor data (Brodrick et al., 2021). For some pixels, however, incorrect or imprecise topographic information could cause those retrievals of the surface properties to produce incorrect interpretations, an issue addressed in Section 5, Discussion. This study characterizes the errors in the solar angles in globally available digital elevation models and recommends steps to mitigate these uncertainties in retrieval of Earth's properties in mountainous terrain.

4 Results

Tables 2 and 3 summarize results for all fine- and coarse-resolution datasets analyzed. Figures 5 and 6 illustrate examples of the results, comparing pairs of variables derived from a fine- and a coarse-resolution image. We include examples from each of the three study sites: Carson River Watershed, Himachal Pradesh in the Indian Himalaya, and Wrangell Mountains in Southeast Alaska.

4.1 Topographic variables independent of solar illumination

Variations in elevation across topography create sloping terrain, so we characterize each pixel by its slope S upward from the horizontal and its aspect A as the direction the slope faces. Slope and aspect combine with the solar angles to create variability in local illumination. The varying terrain also creates the view factors V_Ω, the fraction of the sky hemisphere open above a point. The view factor controls the re-reflection of solar radiation that strikes the surface and the fraction of the diffuse irradiance that reaches the surface. The view factor is also important in modeling the thermal infrared radiation in the mountains (Robledano et al., 2022). The terrain geometry affects the incoming irradiance and the reflected radiation, so the errors in elevation itself are less important than errors in slope, aspect, and view factor. Based on the differences between the fine-resolution and coarse-resolution DEMs, Table 2 shows the RMS error for elevation, differences in elevation between neighbors, slope, aspect, and view factor. Because the differences between the datum sources (Table 1) for elevation exceed 25 m and because we are mostly interested in the internal differences within an elevation grid, we subtract the mean elevation of each grid from that grid's values before calculating the RMS errors for elevation.

Errors in elevation are small fractions of the elevation values themselves, but the errors in slope and aspect indicate significant errors in the differences between elevations of neighboring points. Calculation of the slope S and aspect A of a topographic pixel considers the spatial derivative of elevation Z in two or more directions x and y (Dozier & Frew, 1990), which could be projection coordinates or longitude and latitude distances computed from the coordinates and the dimensions of the ellipsoid:

$$\tan S \equiv |\nabla_Z| = \sqrt{(\partial Z/\partial x)^2 + (\partial Z/\partial y)^2} \quad (1)$$

$$\tan A = \frac{-\partial Z/\partial y}{-\partial Z/\partial x}$$

Including the signs for the numerator and denominator separately enables calculation of aspect A over the full circle. From topographic data, the derivatives are calculated numerically. In a matrix $\mathbf{Z}$ with grid spacing Δh representing topography and the rows running west-east and columns north-south, the derivatives at point $[i, j]$, as calculated by a central difference method, are:

$$\frac{\partial z}{\partial x} = \frac{\boldsymbol{Z}_{i,j+1} - \boldsymbol{Z}_{i,j-1}}{2\Delta h}$$
$$\frac{\partial z}{\partial y} = \frac{\boldsymbol{Z}_{i+1,j} - \boldsymbol{Z}_{i-1,j}}{2\Delta h} \quad (2)$$

The grid spacing Δh is usually known accurately, so assessment of errors that affect topographic radiation depends on the error distribution of the differences between neighboring elevations. We estimated the RMS error of the differences by calculating the numerators of Equation (2) in each direction and then the hypotenuse of the x- and y-direction differences in each pixel. Table 2 shows that the RMS errors in the differences between neighboring elevations are smaller than the RMS errors in the elevations themselves, thereby indicating some spatial coherence in the elevation errors. Otherwise, if the RMS errors of the elevations were indeed independent, then the variance of the differences would be the sum of the variances in the elevations themselves (Weisstein, 2021) and the RMS error of the differences would be $\sqrt{2}$ × the RMS error of the elevations. However, the RMS errors of the differences are much smaller.

Results for the NASADEM and the Copernicus DEM are similar, but both show outliers that translate into outliers in calculating illumination angles.

Insert Table 2 near here

The variability in the data indicates variation within the topographic grid. Figure 5 shows the scatter diagrams for the row in Table 2 that summarizes the statistics for the Copernicus DEM for the Carson River Watershed in the Sierra Nevada. The x-axes represent values from the fine-resolution ASO DEM, the y-axes the values from the globally available Copernicus DEM. For elevation, the spread around the regression in Figure 5a is small. For the other variables, however, the spread is much larger. The outliers in the scatter plots for slope and aspect imply that outliers are present in the local solar angles. Figure 5c shows that some slopes less than 20° in the ASO 3 m DEM correspond to slopes greater than 40° in the Copernicus 1 arcsecond DEM, and conversely some slopes greater than 50° in the finer-resolution DEM correspond to slopes less than 20° in the Copernicus DEM. Similar differences occur in the aspects and view factors.

Insert Figure 5 near here

The regression lines in Figure 5bcd for differences in elevation between neighbors, slope, and aspect are constrained to go through the origin. For elevation (Figure 5a) the

datasets do not use the same datum (Table 1), so the regression includes an intercept. For the view factor (Figure 5c) all values are above about 0.6, so that regression is constrained to go through (1,1) instead of (0,0). In all cases except elevation, the slopes of the regression lines that characterize the relationship between the coarse- and fine-resolution variables are less than 1.0, indicating generally that the Copernicus DEM and NASADEM slightly underestimate the magnitudes. The section on Bias in Table 2 therefore indicates a negative bias in the coarser-resolution datasets (i.e., a regression slope of 0.90 corresponds to a bias of –10%).

Aspect values and their RMS errors must be treated with caution, because aspect has negligible effect on solar radiation when the slope is small but a huge effect when the slope is steep. In our formulation, we follow the right-hand convention that 0° aspect represents south, from which eastward aspects are positive and westward aspects are negative.

4.2 Effect of topography on illumination and reflection

The two crucial topographic variables in order of importance are μ_S, the cosine of the local illumination angle measured from normal to the slope, and V_Ω, the fraction of the hemisphere over a point that is open to the sky. The equation for V_Ω uses the horizon angles H_ϕ for all directions ϕ (Dozier, 2022b):

For slopes facing in the direction toward the Sun, i.e., $\cos(A-\phi) \geq 0$, the limits of integration $[\phi_1, \phi_2]$ being constrained to those azimuths:

$$V_\Omega = \frac{1}{2\pi} \int_{\phi_1}^{\phi_2} \left[\cos S \cos^2 H_\phi + \sin S \cos(A-\phi)\left(\frac{\pi}{2} - H_\phi - \sin H_\phi \cos H_\phi\right)\right] d\phi \qquad (3)$$

For the slopes where $\cos(A-\phi) < 0$, the slope itself might obscure the horizon, so in integrating across those values with the limits of integration corresponding to those azimuths, for each azimuth ϕ, H_ϕ is set to

$$\max\left[H_\phi, \sin^{-1}\left(\sqrt{1 - \frac{1}{1+\cos^2(A-\phi)\tan^2 S}}\right)\right]$$

Over a flat unobstructed surface, $V_\Omega = 1$.

The local illumination angle is related to the topography and the solar illumination geometry as:

$$\mu_S = \max[0, \mu_0 \cos S + \sin\theta_0 \sin S \cos(\phi_0 - A)] \qquad (4)$$

The max function accounts for slopes facing away from the sun by setting $\mu_S = 0$ in situations where the equation would yield $\mu_S < 0$. To account for points where neighboring horizons block the Sun, we also set $\mu_S = 0$ where $\sin H_{\phi_0} \geq \mu_0$.

The variables μ_S and V_Ω affect the relationship between the *apparent* reflectance of the surface and its *intrinsic* reflectance that would be measured independent of any topographic effects (Bair et al., 2022). The apparent reflectance of a topographic surface

involves multiple reflections, especially for bright surfaces such as snow. Let ρ indicate spectral reflectance, omitting a wavelength identifier, and F_{dif} as the fraction of the spectral irradiance that is diffuse. Set the initial irradiance on a horizontal surface to I. The spectral radiation that initially escapes into the overlying hemisphere without being re-reflected is:

$$I_{esc}^{(0)} = IV_\Omega \left[\frac{\mu_S}{\mu_0} (1 - F_{dif}) \rho_{intrinsic}^{(direct)} + F_{dif} \rho_{intrinsic}^{(diffuse)} + (1 - V_\Omega) \left(\rho_{intrinsic}^{(diffuse)} \right)^2 \right] \quad (5)$$

The equation assumes that $\rho_{intrinsic}$ is approximately isotropic averaged over the field of view, it neglects atmospheric attenuation within the topography, and it ignores variation in albedo and irradiance within the neighborhood. The superscripts designate the reflectance to direct vs. diffuse irradiance. The right-most term inside the brackets accounts for reflected radiation within a point's field of view impinging on the point. The direct and diffuse spectral albedos might differ slightly, for example for snow.

Not all the initially reflected radiation escapes into the overlying hemisphere. Instead, some of it re-reflects and eventually escapes or is trapped by the topography, in which case it is subject to internal reflection. At the first iteration, its value is:

$$I_{internal}^{(0)} = I_{esc}^{(0)} \left(\frac{1 - V_\Omega}{V_\Omega} \right). \quad (6)$$

To account for multiple reflections, at each reflection the value of the incident radiation is multiplied by the fraction $(1 - V_\Omega)$ that accounts for the reflection remaining within the topography, the fraction V_Ω that escapes, and the intrinsic spectral reflectance. An orders-of-scattering approach to the multiple reflections lets some reflected radiation escape at each iteration n and some remains available for re-reflection:

$$\begin{aligned} \text{escaped } I_{esc}^{(n)} &= I_{internal}^{(n-1)} \rho_{intrinsic}^{(diffuse)} V_\Omega \\ \text{remaining } I_{internal}^{(n)} &= I_{internal}^{(n-1)} \rho_{intrinsic}^{(diffuse)} (1 - V_\Omega) \end{aligned} \quad (7)$$

This series converges in a half dozen iterations because $I_{internal}^{(n)}$ declines in proportion to $(1 - V_\Omega)^n$. The apparent reflectance for the pixel is $\rho_{apparent} = \sum I_{esc} / I$.

4.3 Errors in estimating μ_S, the cosine of local illumination

RMS errors and outliers in the topographic variables combine with the solar illumination geometry to propagate into the calculation of each pixel's illumination. The most important variable whose accuracy affects the interpretation of the remotely sensed signal is the cosine of the local illumination angle. The ratio μ_S / μ_0 appears in Equation (5), but μ_0 is usually known accurately. The view factor V_Ω affects the diffuse irradiance from the sky and the internal reflections within the topography.

Therefore, the accuracy of the cosine of illumination from the DEM affects our ability to calculate or correct for the topographic effects. For example, attempting to invert Equation (5) to solve for $\rho_{intrinsic}$ would involve the ratio μ_0 / μ_S; uncertainty in the denominator of a fraction often has significant consequences, especially if the denominator is small (Richter & Schläpfer, 2021, chapter 7). Table 3 shows the RMS errors for the cosine of illumination, along with the fraction of the terrain that is shadowed, for the dates in

Figure 2 that extend from the winter to the summer solstice in equal changes of the solar declination. The RMS error for μ_S varies inversely with the value of μ_0; the errors in slope S and aspect A have a greater effect when μ_0 is smaller.

Insert Table 3 near here

The full extent of errors in the results indicates issues with outliers that the RMS errors do not reveal. Figure 6 shows scatter diagrams of μ_s calculated from the Copernicus DEM vs μ_s calculated from the Alaska IFSAR DEM. On all dates but particularly early in the year, some pixels that are illuminated ($\mu_S \gg 0$) in the Copernicus DEM are in the dark ($\mu_S < 0.1$) in the Alaska IFSAR DEM. Similarly, some pixels that the Alaska IFSAR DEM shows to be illuminated are dark in the Copernicus DEM. A popular text on surveying published six decades ago (Davis et al., 1966) calls these kinds of mistakes "blunders" rather than "errors," because they cannot be characterized by an error distribution.

5 Discussion

Although errors or blunders in the NASADEM and Copernicus DEM are minor compared to the elevation values, their impact on remote sensing can be large. Thus, the small dispersion around the 1:1 line in the scatter diagram for elevation in Figure 5a translates to much greater dispersion in the slope, aspect, and view factor (Figure 5cde), which in turn translates to large dispersion in the illumination angles that Figure 6 shows. Therefore, small errors in slope or aspect can then significantly affect estimated reflectance, especially wherever μ_S is small.

Algorithms to retrieve surface properties differ in their sensitivities to topographic uncertainty. The effect is mostly a shift in spectral reflectance magnitude, so algorithms that rely on relative spectral shapes may escape significant harm. These include detection of materials based on diagnostic spectral absorptions, as in mineral identification (Clark et al., 2003). On the other hand, studies that rely on absolute radiometry, such as surface energy balance investigations (Wang et al., 2015) or retrieval of snow properties (Bohn et al., 2021), could be more severely affected. Moreover, errors in μ_S change the estimated balance between diffuse and direct illumination onto the surface. Therefore, they can distort the estimated reflectance spectrum in visible wavelengths, harming snow or vegetation studies that rely on features in this spectral range.

Solar illumination geometry in mountains affects current satellite imagery from Landsat 8/9 and Sentinel-2A/B, it affects data from imaging spectrometers EnMAP (Chabrillat et al., 2020) and EMIT (Connelly et al., 2021), and it will affect data from future missions SBG (Cawse-Nicholson et al., 2021; Stavros et al., 2022) and CHIME (Rast et al., 2021). Locally, fine-resolution DEMs will be available from lidar, InSAR, or structure-from-motion deployed from drones or aircraft, and slightly coarser DEMs will be available using structure-from-motion from spaceborne data. However, the prospect is unlikely for globally available data to accurately estimate the solar illumination geometry for these imaging satellites. A chapter in *Thriving on our Changing Planet* (National Academies of Science, Engineering, & Medicine, 2018, p. 513) identifies applications that "would benefit from multibeam, space-based lidar to obtain global coverage of bare-earth topography and of the biomass/canopy at <<5 m spatial and 0.1 m vertical resolutions." However, no such

recommendation carried through to that report's Executive Summary, and no future NASA mission is in the planning stages.

Therefore, we face a future where the globally available DEMs at ~30 m resolution are what we have now, at least through the launches and initial few years of the spectrometers SBG and CHIME and future versions of Landsat and Sentinel. If we could trust the variables calculated from DEMs and consider only the RMS errors, we could implement topographic correction algorithms that estimate $\rho_{intrinsic}$ from measurements of atmospherically corrected $\rho_{apparent}$ and thereby recover the geophysical and biological properties of the surface that govern spectral reflectance, with known uncertainty. However, we face the problem of outliers in the calculations of μ_S and less crucially V_Ω, so applying any correction algorithm globally on entire images would produce some incorrect, thus misleading, retrievals.

Strategies to mitigate the impact of topographic errors in processing and distributing image data and products must be considered. The list is deliberately terse; any bullet point could be expanded to a whole journal article:

- In the basis documents for algorithms for geophysical and biological products, assess their sensitivity to uncertainty in illumination geometry and distinguish between topographic effects that change the spectral shape of the signal vs. those that change the magnitude only (Lamare et al., 2020).
- Gain a better understanding of the use of shade endmembers (Adams et al., 1986) in spectral mixture analysis, which implicitly acknowledge the limitations of available DEMs by solving for an illumination adjustment on modeled values of a pixel's reflectance.
- Understand the relative magnitudes of topographic effects on angular properties of the reflectance vs. the effects of illumination and viewing geometry on the intrinsic reflectance (Roupioz et al., 2014; Schaepman-Strub et al., 2006).
- Develop and validate image processing methods that identify pixels where errors in the underlying DEM would lead to incorrect calculations of the illumination geometry, for example detection of shadowed terrain (Hagolle et al., 2017; Hollstein et al., 2016; Shahtahmassebi et al., 2013).
- Avoid exclusively prescribing global topographic correction solutions. Preserve the flexibility, within the mission science data system, for investigators to apply new regional DEMs of higher accuracy as these become available, or to ignore topography.

In the longer term, future research may reduce DEM-induced reflectance errors through strategies such as the following:

- Implement topographic corrections in superpixels, thereby smoothing out the errors in individual pixels (Gilmore et al., 2011).
- Continue efforts to improve DEMs globally, especially in mountainous areas, for example the USGS 3D elevation program in the U.S. (Stoker & Miller, 2022).
- Examine and validate novel methods to estimate illumination geometry directly from images, for example by simultaneously solving for unknown atmospheric and

topographic properties in retrieval of surface reflectance from top-of-atmosphere radiances.

6 Conclusions

Our analyses show that calculations in the globally available DEMs miss shadows and consistently underestimate cosines of solar illumination angles, RMS error increasing with solar zenith angle. Analyzing imagery of Earth's mountains from current and future missions requires addressing the uncertainty introduced by errors and outliers in the DEMs on algorithms that retrieve surface properties from measurements of the apparent spectral reflectance. Intriguing potential improvements lie in assessing the uncertainties in retrievals of geophysical and biological properties and in novel methods to gain information about topography from the imagery itself.

Acknowledgments

All authors declare no real or perceived financial conflicts of interests. We appreciate reviews by Olivier Hagolle, Ghislain Picard, and an anonymous referee. A portion of this work was carried out at the Jet Propulsion Laboratory, California Institute of Technology, under NASA Award 80NM0018D0004. Amazon Web Services (AWS) Cloud Credit for Research Program provided computing support. The UC Santa Barbara Library supports publishing of research data for the campus through the Dryad Data Repository. The following authors acknowledge specific support: JD, NASA Award 80NSSC21K0620; EHB, NASA Awards 80NSSC21K0997, 80NSSC20K1722, 80NSSC20K1349, and 80NSSC18K1489; THP, NASA Award 80NSSC19K0645.

Open Research

We have assembled all elevation data used in this research in Dryad (Dozier et al., 2022) under the Creative Commons Zero Waiver. Those elevation files include splicing and cropping to match areas of fine and coarse resolution, so within each region (Carson River, Himachal Pradesh, Wrangell Mountains) the DEMs at different resolutions cover the same area, thereby enabling the comparison of the same topographic variables calculated from different data sources.

Public sources of the data are:

- NASADEM tiles are available from the U.S. Geological Survey Land Processes DAAC Data Pool (NASA JPL, 2020). Registration is required but is free.
- Copernicus DEMs customized to specific latitude-longitude quadrilaterals are available from Open Topography (European Space Agency, 2021).
- Airborne Snow Observatories Inc. provided the snow-off elevation data at 3 m spatial resolution for the Carson River Watershed. The data are available in Dozier et al. (2022).
- The Alaska elevation data, acquired by airborne interferometric synthetic aperture radar, are available from the U.S. Geological Survey (USGS EROS Archive, 2018).
- Tiles for the High Mountain Asia 8 m DEM are available at the National Snow and Ice Data Center (Shean, 2017).
- Global grids of the EGM96 and EGM2008 Geoids are available from Agisoft (2008).

Computer codes for calculating solar illumination geometry (Dozier, 2020) and topographic horizons and other terrain parameters (Dozier, 2022a) are available from the MATLAB Central file exchange. Code for reprojecting raster data is on GitHub (Dozier, 2021). All codes are published and copyrighted under a free re-use license, even for commercial purposes.

References

Adams, J. B., Smith, M. O., & Johnson, P. E. (1986). Spectral mixture modeling: A new analysis of rock and soil types at the Viking Lander 1 Site. *Journal of Geophysical Research: Solid Earth, 91*, 8098-8112. https://doi.org/10.1029/JB091iB08p08098

Agisoft. (2008). *Global Geoid Models* [Datasets]. https://www.agisoft.com/downloads/geoids/

Bair, E. H., Stillinger, T., & Dozier, J. (2021). Snow Property Inversion from Remote Sensing (SPIReS): A generalized multispectral unmixing approach with examples from MODIS and Landsat 8 OLI. *IEEE Transactions on Geoscience and Remote Sensing, 59*, 7270-7284. https://doi.org/10.1109/TGRS.2020.3040328

Bair, E. H., Dozier, J., Stern, C., LeWinter, A., Rittger, K., Savagian, A., et al. (2022). Divergence of apparent and intrinsic snow albedo over a season at a sub-alpine site with implications for remote sensing. *The Cryosphere, 16*, 1765-1778. https://doi.org/10.5194/tc-16-1765-2022

Barros, A. P. (2013). Orographic precipitation, freshwater resources, and climate vulnerabilities in mountainous regions. In R. Pielke (Ed.), *Climate Vulnerability: Understanding and Addressing Threats to Essential Resources* (pp. 57-78). Oxford: Academic Press. https://doi.org/10.1016/B978-0-12-384703-4.00504-9

Bogan, S. A., Antonarakis, A. S., & Moorcroft, P. R. (2019). Imaging spectrometry-derived estimates of regional ecosystem composition for the Sierra Nevada, California. *Remote Sensing of Environment, 228*, 14-30. https://doi.org/10.1016/j.rse.2019.03.031

Bohn, N., Painter, T. H., Thompson, D. R., Carmon, N., Susiluoto, J., Turmon, M. J., et al. (2021). Optimal estimation of snow and ice surface parameters from imaging spectroscopy measurements. *Remote Sensing of Environment, 264*, 112613. https://doi.org/10.1016/j.rse.2021.112613

Brodrick, P. G., Thompson, D. R., Fahlen, J. E., Eastwood, M. L., Sarture, C. M., Lundeen, S. R., et al. (2021). Generalized radiative transfer emulation for imaging spectroscopy reflectance retrievals. *Remote Sensing of Environment, 261*, 112476. https://doi.org/10.1016/j.rse.2021.112476

Buckley, S. (2020). NASADEM: Creating a new NASA digital elevation model and associated products. NASA. https://earthdata.nasa.gov/esds/competitive-programs/measures/nasadem

Cawse-Nicholson, K., Townsend, P. A., Schimel, D., Assiri, A. M., Blake, P. L., Buongiorno, M. F., et al. (2021). NASA's surface biology and geology designated observable: A perspective on surface imaging algorithms. *Remote Sensing of Environment, 257*, 112349. https://doi.org/10.1016/j.rse.2021.112349

Chabrillat, S., Guanter, L., Segl, K., Foerster, S., Fischer, S., Rossner, G., et al. (2020). *The EnMAP German spaceborne imaging spectroscopy mission: update and highlights of recent preparatory activities.* Paper presented at the International Geoscience and Remote Sensing Symposium (IGARSS 2020). https://doi.org/10.1109/IGARSS39084.2020.9324006

Clark, R. N., Swayze, G. A., Livo, K. E., Kokaly, R. F., Sutley, S. J., Dalton, J. B., et al. (2003). Imaging spectroscopy: Earth and planetary remote sensing with the USGS Tetracorder and expert systems. *Journal of Geophysical Research: Planets, 108*, 5131. https://doi.org/10.1029/2002JE001847

Connelly, D. S., Thompson, D. R., Mahowald, N. M., Li, L., Carmon, N., Okin, G. S., & Green, R. O. (2021). The EMIT mission information yield for mineral dust radiative forcing. *Remote Sensing of Environment, 258*, 112380. https://doi.org/10.1016/j.rse.2021.112380

Davis, R. E., Foote, F. S., & Kelly, J. W. (1966). *Surveying Theory and Practice* (5th ed.). New York: McGraw-Hill.

Dozier, J., & Frew, J. (1990). Rapid calculation of terrain parameters for radiation modeling from digital elevation data. *IEEE Transactions on Geoscience and Remote Sensing, 28*, 963-969. https://doi.org/10.1109/36.58986

Dozier, J. (2020). Sun position: functions for declination, solar longitude, radius vector, equation of time, times of sunrise and sunset, sun angles and azimuths. Natick, MA: MATLAB Central File Exchange. https://www.mathworks.com/matlabcentral/fileexchange/74939-sun-position.

Dozier, J. (2021). Raster reprojection. https://github.com/DozierJeff/RasterReprojection.

Dozier, J. (2022a). Topographic horizons: angles to the horizons from an elevation grid with options for parallelism (Version 4.4). Natick, MA: MATLAB Central File Exchange. https://www.mathworks.com/matlabcentral/fileexchange/94800-topographic-horizons.

Dozier, J. (2022b). Revisiting topographic horizons in the era of big data and parallel computing. *IEEE Geoscience and Remote Sensing Letters, 19*, 8024605. https://doi.org/10.1109/LGRS.2021.3125278

Dozier, J., Baskaran, L., & Painter, T. H. (2022). *Topographic data to support the analysis of error and uncertainty that degrade topographic corrections of remotely sensed data* [Distributed by Dryad]. https://doi.org/10.25349/D98896

European Space Agency. (2021). *Copernicus Global Digital Elevation Model* [Dataset distributed by Open Topography]. https://doi.org/10.5069/G9028PQB

Farr, T. G., Rosen, P. A., Caro, E., Crippen, R., Duren, R., Hensley, S., et al. (2007). The Shuttle Radar Topography Mission. *Reviews of Geophysics, 45*, RG2004. https://doi.org/10.1029/2005RG000183

Gilmore, M. S., Thompson, D. R., Anderson, L. J., Karamzadeh, N., Mandrake, L., & Castaño, R. (2011). Superpixel segmentation for analysis of hyperspectral data sets, with application to Compact Reconnaissance Imaging Spectrometer for Mars data, Moon Mineralogy Mapper data, and Ariadnes Chaos, Mars. *Journal of Geophysical Research: Planets, 116*, E07001. https://doi.org/10.1029/2010JE003763

Guth, P. L., & Geoffroy, T. M. (2021). LiDAR point cloud and ICESat-2 evaluation of 1 second global digital elevation models: Copernicus wins. *Transactions in GIS, 25*, 2245-2261. https://doi.org/10.1111/tgis.12825

Hagolle, O., Huc, M., Desjardins, C., Auer, S., & Richter, R. (2017). *MAJA algorithm theoretical basis document (1.0)* MAJA-TN-WP2-030 V1.0): CNES/DLR. https://doi.org/10.5281/zenodo.1209633

Hollstein, A., Segl, K., Guanter, L., Brell, M., & Enesco, M. (2016). Ready-to-use methods for the detection of clouds, cirrus, snow, shadow, water and clear sky pixels in Sentinel-2 MSI images. *Remote Sensing, 8*, 666. https://doi.org/10.3390/rs8080666

Immerzeel, W. W., Lutz, A. F., Andrade, M., Bahl, A., Biemans, H., Bolch, T., et al. (2020). Importance and vulnerability of the world's water towers. *Nature, 577*, 364-369. https://doi.org/10.1038/s41586-019-1822-y

Kirschbaum, D., Kapnick, S. B., Stanley, T., & Pascale, S. (2020). Changes in extreme precipitation and landslides over High Mountain Asia. *Geophysical Research Letters, 47*, e2019GL085347. https://doi.org/10.1029/2019GL085347

Kruse, F. A., Lefkoff, A. B., Boardman, J. W., Heidebrecht, K. B., Shapiro, A. T., Barloon, P. J., & Goetz, A. F. H. (1993). The spectral image processing system (SIPS)—interactive visualization and analysis of imaging spectrometer data. *Remote Sensing of Environment, 44*, 145-163. https://doi.org/10.1016/0034-4257(93)90013-N

Lamare, M., Dumont, M., Picard, G., Larue, F., Tuzet, F., Delcourt, C., & Arnaud, L. (2020). Simulating optical top-of-atmosphere radiance satellite images over snow-covered rugged terrain. *The Cryosphere, 14*, 3995-4020. https://doi.org/10.5194/tc-14-3995-2020

Mankin, J. S., Viviroli, D., Singh, D., Hoekstra, A. Y., & Diffenbaugh, N. S. (2015). The potential for snow to supply human water demand in the present and future. *Environmental Research Letters, 10*, 114016. https://doi.org/10.1088/1748-9326/10/11/114016

Moody, J. A., & Martin, D. A. (2001). Post-fire, rainfall intensity–peak discharge relations for three mountainous watersheds in the western USA. *Hydrological Processes, 15*, 2981-2993. https://doi.org/10.1002/hyp.386

Mulder, V. L., de Bruin, S., Weyermann, J., Kokaly, R. F., & Schaepman, M. E. (2013). Characterizing regional soil mineral composition using spectroscopy and geostatistics. *Remote Sensing of Environment, 139*, 415-429. https://doi.org/10.1016/j.rse.2013.08.018

NASA & METI. (2019). *ASTGTM V003: ASTER Global Digital Elevation Model 1 arc second* [Distributed by USGS Land Processes DAAC]. https://doi.org/10.5067/ASTER/ASTGTM.003

NASA JPL. (2020). *NASADEM Merged DEM Global 1 arc second V001* [Dataset distributed by USGS Land Processes DAAC]. https://doi.org/10.5067/MEaSUREs/NASADEM/NASADEM_HGT.001

National Academies of Sciences, Engineering, & Medicine. (2018). *Thriving on Our Changing Planet: A Decadal Strategy for Earth Observation from Space*. Washington, DC: National Academies Press. https://doi.org/10.17226/24938

NOAA. (no date). NOAA solar calculator. Boulder, CO: NOAA Earth System Research Laboratory. http://www.esrl.noaa.gov/gmd/grad/solcalc/

Painter, T. H., Seidel, F. C., Bryant, A. C., Skiles, S. M., & Rittger, K. (2013). Imaging spectroscopy of albedo and radiative forcing by light-absorbing impurities in mountain snow. *Journal of Geophysical Research-Atmospheres, 118*, 9511-9523. https://doi.org/10.1002/jgrd.50520

Painter, T. H., Berisford, D. F., Boardman, J. W., Bormann, K. J., Deems, J. S., Gehrke, F., et al. (2016). The Airborne Snow Observatory: Fusion of scanning lidar, imaging spectrometer, and physically-based modeling for mapping snow water equivalent and snow albedo. *Remote Sensing of Environment, 184*, 139-152. https://doi.org/10.1016/j.rse.2016.06.018

Rast, M., Nieke, J., Adams, J., Isola, C., & Gascon, F. (2021). *Copernicus Hyperspectral Imaging Mission for the Environment (CHIME).* Paper presented at the IEEE International Geoscience and Remote Sensing Symposium (IGARSS 2021). https://doi.org/10.1109/IGARSS47720.2021.9553319

Richter, R., & Schläpfer, D. (2021). *ATCOR Theoretical Background*. CH-9500 Wil, Switzerland: ReSe Applications. https://www.rese-apps.com/pdf/atcor_atbd.pdf

Robledano, A., Picard, G., Arnaud, L., Larue, F., & Ollivier, I. (2022). Modelling surface temperature and radiation budget of snow-covered complex terrain. *The Cryosphere, 16*, 559-579. https://doi.org/10.5194/tc-16-559-2022

Roupioz, L., Nerry, F., Jia, L., & Menenti, M. (2014). Improved surface reflectance from remote sensing data with sub-pixel topographic information. *Remote Sensing, 6*, 10356-10374. https://doi.org/10.3390/rs61110356

Schaepman-Strub, G., Schaepman, M. E., Painter, T. H., Dangel, S., & Martonchik, J. V. (2006). Reflectance quantities in optical remote sensing—definitions and case studies. *Remote Sensing of Environment, 103*, 27-42. https://doi.org/10.1016/j.rse.2006.03.002

Shahtahmassebi, A. R., Yang, N., Wang, K., Moore, N., & Shen, Z. (2013). Review of shadow detection and de-shadowing methods in remote sensing. *Chinese Geographical Science, 23*, 403-420. https://doi.org/10.1007/s11769-013-0613-x

Shean, D. E., Alexandrov, O., Moratto, Z. M., Smith, B. E., Joughin, I. R., Porter, C., & Morin, P. (2016). An automated, open-source pipeline for mass production of digital elevation models (DEMs) from very-high-resolution commercial stereo satellite imagery. *ISPRS Journal of Photogrammetry and Remote Sensing, 116*, 101-117. https://doi.org/10.1016/j.isprsjprs.2016.03.012

Shean, D. E. (2017). *High Mountain Asia 8-meter DEM mosaics derived from optical imagery, Version 1* [Dataset distributed by National Snow and Ice Data Center]. https://doi.org/10.5067/KXOVQ9L172S2

Shugart, H. H., French, N. H. F., Kasischke, E. S., Slawski, J. J., Dull, C. W., Shuchman, R. A., & Mwangi, J. (2001). Detection of vegetation change using reconnaissance imagery. *Global Change Biology, 7*, 247-252. https://doi.org/10.1046/j.1365-2486.2001.00379.x

Space Applications Centre. (2017). *Spectrum of India*. Bangalore: Indian Space Research Organisation.

Stavros, E. N., Chrone, J., Cawse-Nicholson, K., Freeman, A., Glenn, N. F., Guild, L., et al. (2022). Designing an observing system to study the Surface Biology and Geology (SBG) of the Earth in the 2020s. *Journal of Geophysical Research: Biogeosciences*, e2021JG006471. https://doi.org/10.1029/2021JG006471

Stoker, J., & Miller, B. (2022). The accuracy and consistency of 3D elevation program data: a systematic analysis. *Remote Sensing, 14*, 940. https://doi.org/10.3390/rs14040940

USGS EROS Archive. (2018). *Digital Elevation - Interferometric Synthetic Aperture Radar (IFSAR) - Alaska* [Distributed by Earth Resources Observation and Science (EROS) Center]. https://doi.org/10.5066/P9C064CO

Uuemaa, E., Ahi, S., Montibeller, B., Muru, M., & Kmoch, A. (2020). Vertical accuracy of freely available global digital elevation models (ASTER, AW3D30, MERIT, TanDEM-X, SRTM, and NASADEM). *Remote Sensing, 12*, 3482. https://doi.org/10.3390/rs12213482

Viviroli, D., Dürr, H. H., Messerli, B., Meybeck, M., & Weingartner, R. (2007). Mountains of the world, water towers for humanity: Typology, mapping, and global significance. *Water Resources Research, 43*, W07447. https://doi.org/10.1029/2006WR005653

Wang, D., Liang, S., He, T., & Shi, Q. (2015). Estimating clear-sky all-wave net radiation from combined visible and shortwave infrared (VSWIR) and thermal infrared (TIR) remote sensing data. *Remote Sensing of Environment, 167*, 31-39. https://doi.org/10.1016/j.rse.2015.03.022

Weisstein, E. W. (2021). Normal difference distribution. Wolfram MathWorld. https://mathworld.wolfram.com/NormalDifferenceDistribution.html

Wrzesien, M. L., Pavelsky, T. M., Durand, M. T., Dozier, J., & Lundquist, J. D. (2019). Characterizing biases in mountain snow accumulation from global datasets. *Water Resources Research, 55*, 9873-9891. https://doi.org/10.1029/2019WR025350

Table Captions

Table 1. Information sources for digital elevation models used in the analysis.

Table 2. RMS error statistics for topographic variables that are independent of solar illumination.

Table 3. Shadowed fraction and RMS error of μ_S (cosine solar illumination) for each date in each dataset, varying monotonically with the solar zenith angle $\mu_0 = \cos\theta_0$.

Figure Captions

Figure 1. Example of the elevation sources for the Carson River Watershed. The left image shows the Copernicus DEM, whose spatial resolution is 1 arcsecond; the right image shows a segment of the ASO 3 m DEM, corresponding to the red rectangle in the left image. Both images are in a UTM projection, Zone 11N.

Figure 2. Dates and their solar declinations (degrees) used in the analysis, spaced in equal latitude intervals from the winter solstice to the summer solstice (NOAA, no date, solar calculator).

Figure 3. Values of μ_S (cosine of local solar illumination angle, including shadowing by horizons) over the Indian Himalaya at 10:45 am on the dates shown in Figure 2, from the winter to the summer solstice. Solar zenith angles varied from winter to summer: 60°, 55°, 48°, 41°, 33°, 27°, 23°. The area coincides with 9 flight lines by AVIRIS-NG during the 2016 ISRO-NASA campaign. The solar illumination values are calculated from the High Mountain Asia 8 m DEM, whose tiles are in an Albers Equaconic Projection, an equal area projection with origin 36°N 85°E and standard parallels 25°N and 47°N.

Figure 4. (a) Top-of-atmosphere reflectance ($\pi \times$ radiance/irradiance) in Landsat 8 OLI band 5 (851-879 nm) in the Indian Himalaya acquired on 22 February 2016 at UTC 05:24. (b) Cosine μ_S of the solar illumination, including cast shadows, at the same time over a NASADEM matching the Landsat image. The solar zenith angle on a flat surface was 49.3°. (c) Scatter density diagram with the Landsat reflectance on the vertical axis and μ_S on the horizontal axis. The colors show density of points, with bright yellow indicating high concentrations. The blank area eliminates the values within 1 RMS error of the linear regression $f(x) = ax + b$. (d) Probability density functions (pdf) of the reflectance values in two illumination categories, $\mu_S < 0.2$ and $\mu_S > 0.87$, covering the same fractions (14%) of the image's values.

Figure 5. Detailed illustration supporting one row in Table 2 for the Copernicus DEM in the Carson River Watershed in the Sierra Nevada. The *x*-axes show data for the ASO 3 m DEM; the *y*-axes show the same information derived from the Copernicus DEM, with both DEMs reprojected to a common size and projection. Aspect angles represent south as 0°, eastward positive, westward negative, and therefore consistent with a right-hand coordinate system. Regression lines in the figure and statistics in Table 2 are based on the whole topographic grid, but just 100,000 points are randomly selected for the illustrative scatter plots.

685 **Figure 6.** Detailed illustration supporting the Wrangell Mountains group in Table 3 for the
686 Copernicus DEM. All axes show values of μ_S, the cosine of local illumination, varying with the dates
687 that Figure 2 shows. Points along either the x- or y-axis identify locations that are shadowed in one
688 DEM and illuminated in the other. Regression lines in the figure and statistics in Table 3 are based
689 on all pixels in the data, but just 100,000 points are randomly selected for the illustrative scatter
690 density plots. Note that the yellow (bright) values in the scatter density plots migrate to higher
691 values of μ_S as the solar declination moves northward.

Figure 1.

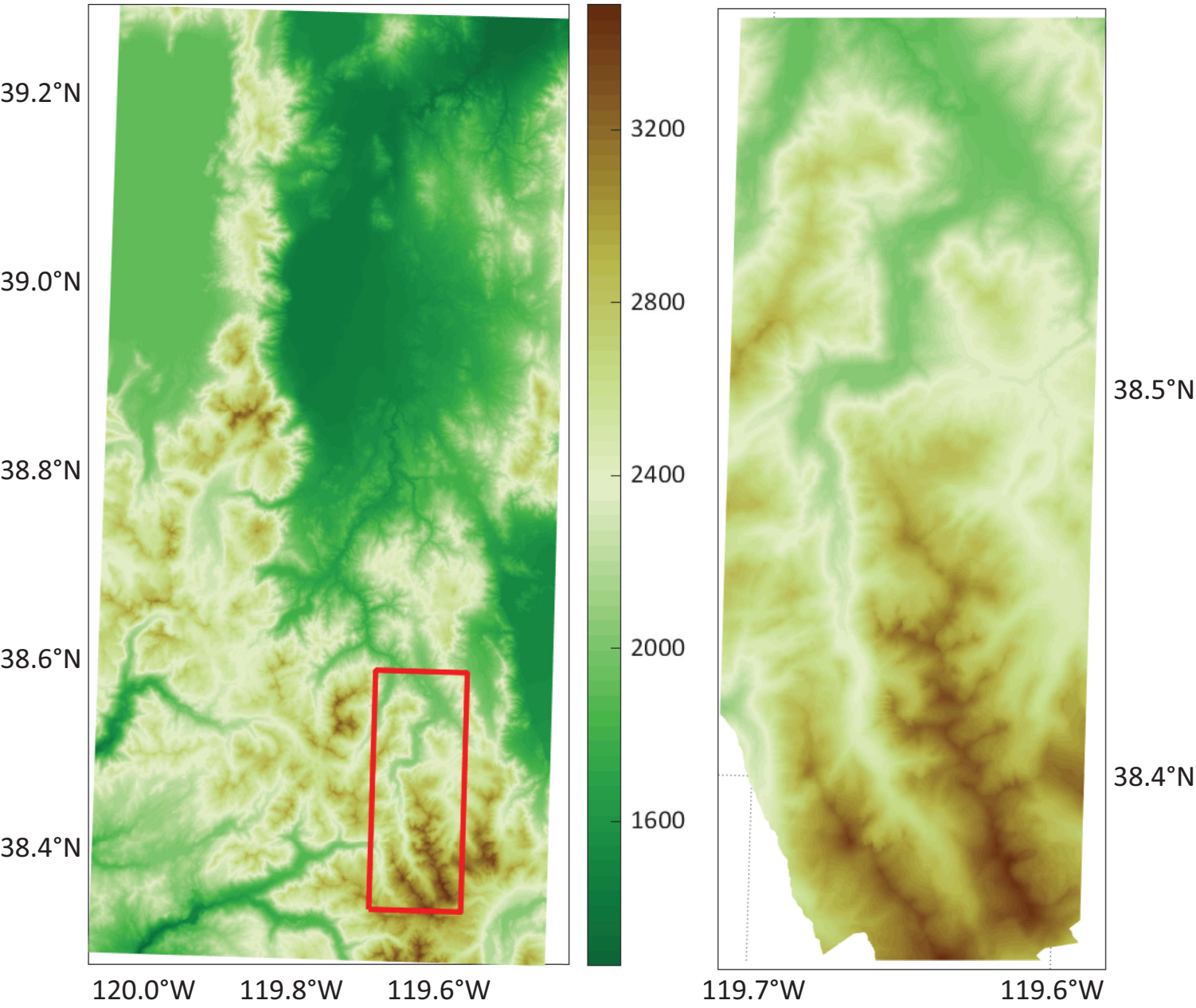
39.2°N
39.0°N
38.8°N
38.6°N
38.4°N
3200
2800
2400
2000
1600
38.5°N
38.4°N
120.0°W
119.8°W
119.6°W
119.7°W
119.6°W

Figure 2.

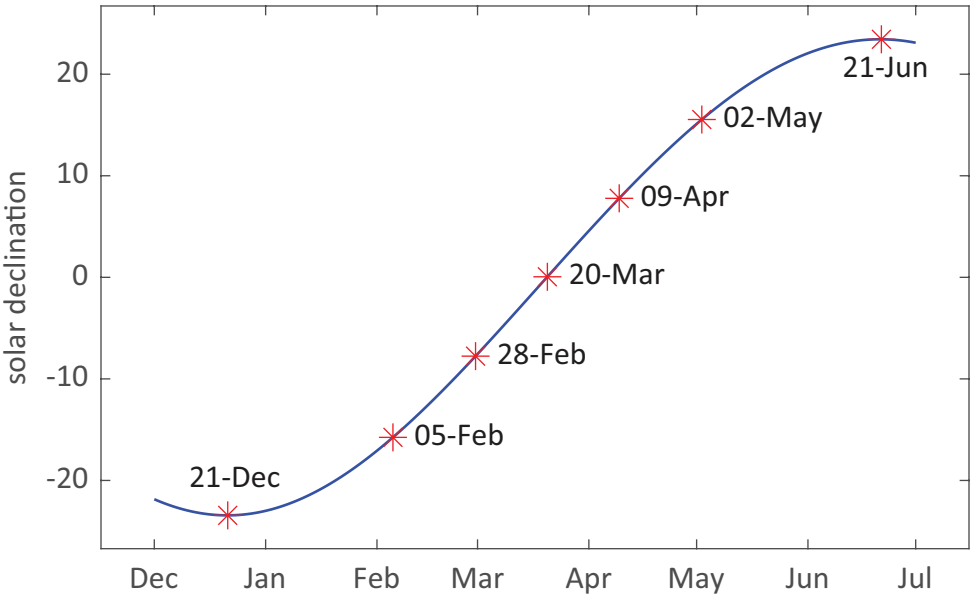
solar declination
20
10
0
-10
-20
Dec
Jan
Feb
Mar
Apr
May
Jun
Jul
21-Dec
05-Feb
28-Feb
20-Mar
09-Apr
02-May
21-Jun

Figure 3.

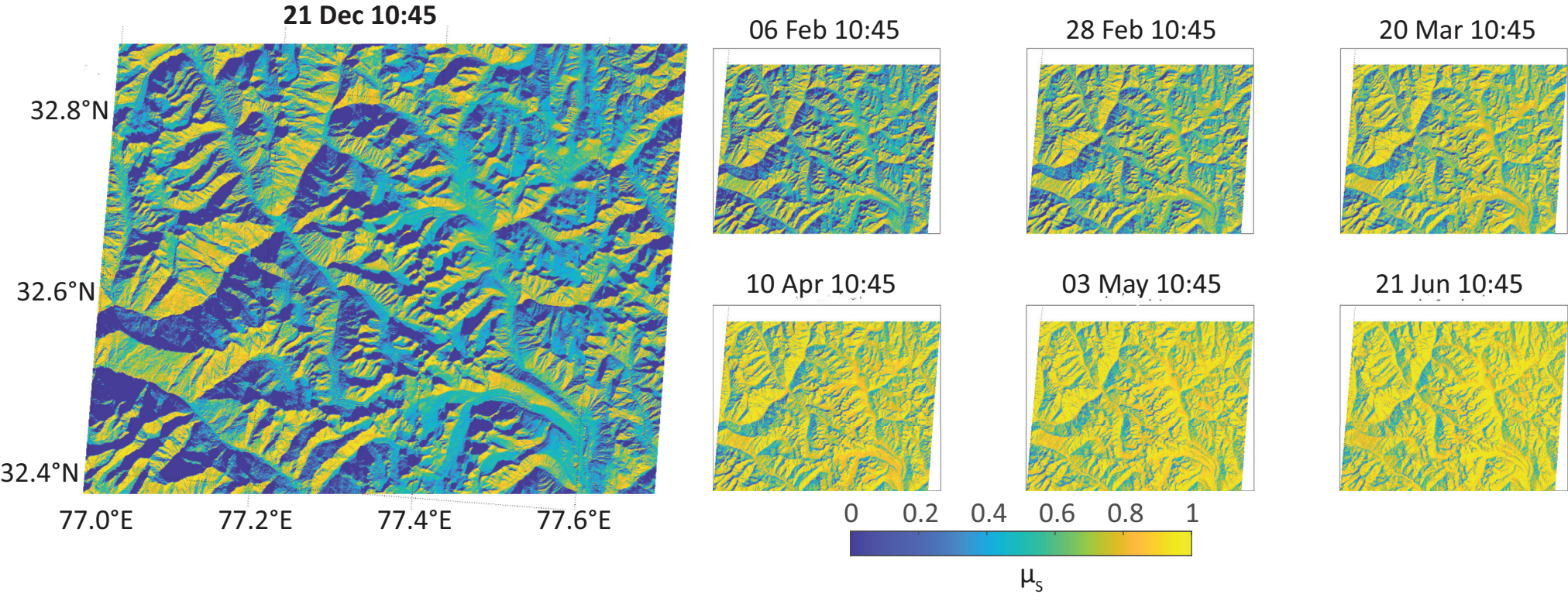
21 Dec 10:45
06 Feb 10:45
28 Feb 10:45
20 Mar 10:45
10 Apr 10:45
03 May 10:45
21 Jun 10:45
32.8°N
32.6°N
32.4°N
77.0°E
77.2°E
77.4°E
77.6°E
0
0.2
0.4
0.6
0.8
1
μs

Figure 4.

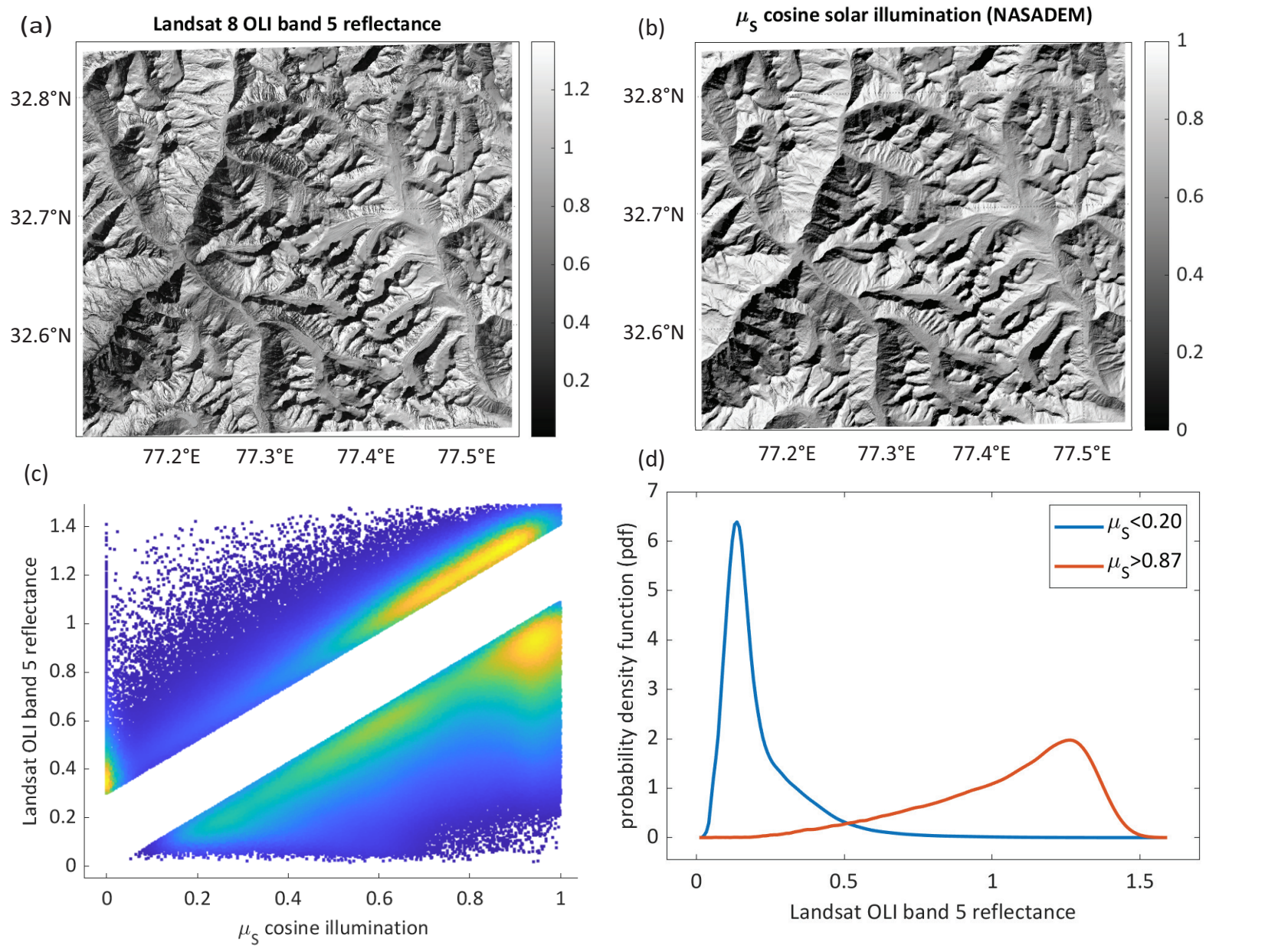
(a)
Landsat 8 OLI band 5 reflectance
32.8°N
32.7°N
32.6°N
77.2°E
77.3°E
77.4°E
77.5°E
1.2
1
0.8
0.6
0.4
0.2
(b)
μ_s cosine solar illumination (NASADEM)
32.8°N
32.7°N
32.6°N
77.2°E
77.3°E
77.4°E
77.5°E
1
0.8
0.6
0.4
0.2
0
(c)
Landsat OLI band 5 reflectance
1.4
1.2
1
0.8
0.6
0.4
0.2
0
0
0.2
0.4
0.6
0.8
1
μ_s cosine illumination
(d)
probability density function (pdf)
7
6
5
4
3
2
1
0
0
0.5
1
1.5
Landsat OLI band 5 reflectance
μ_s<0.20
μ_s>0.87

Figure 5.

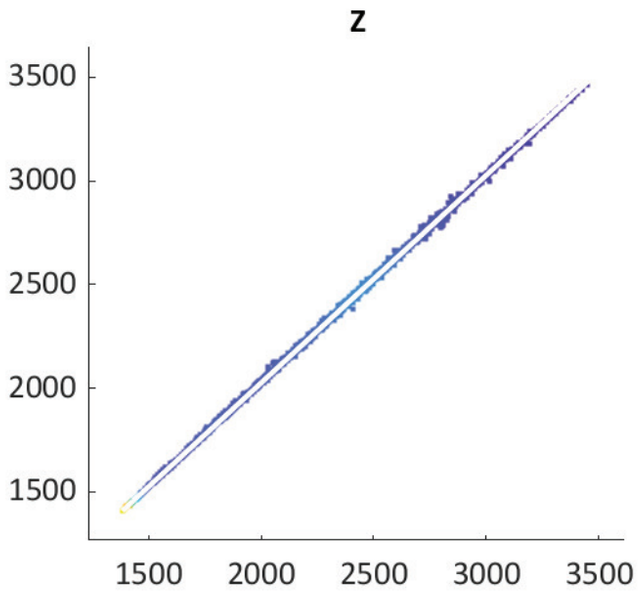

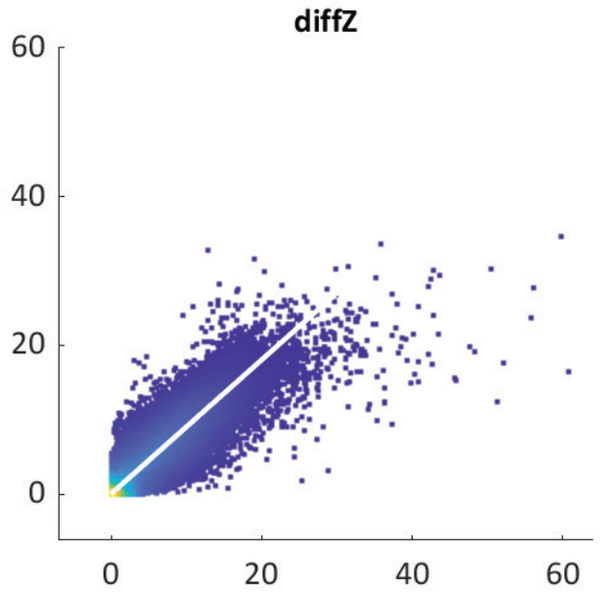

x-axes represent values from the fine-resolution (3 m) data, sampled to the common 10 m resolution.
y-axes represent the coarse-resolution data (1 arcsec), sampled to the same 10 m resolution.

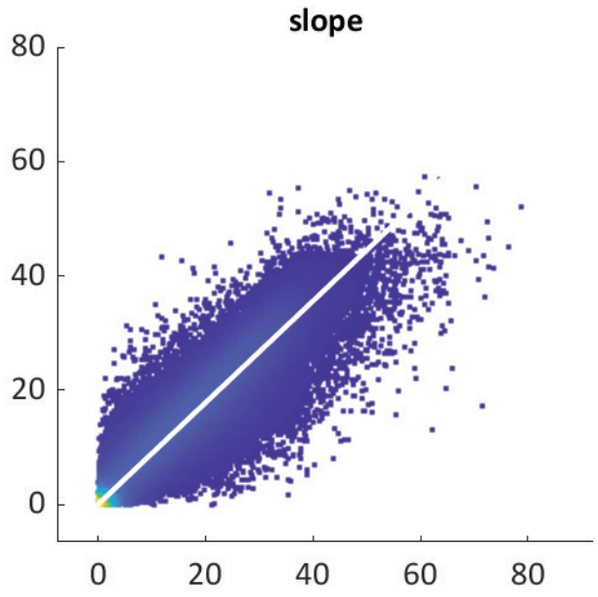

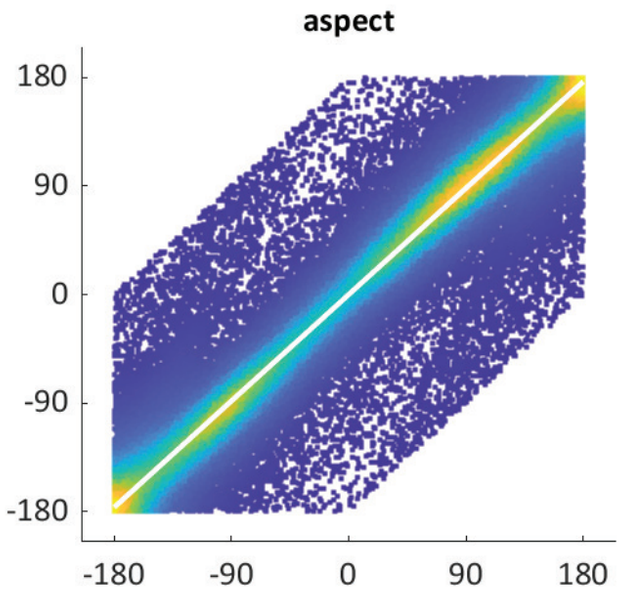

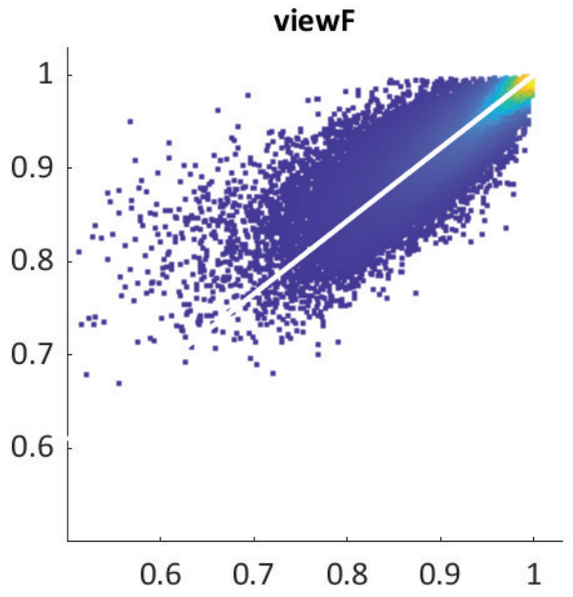

Figure 6.

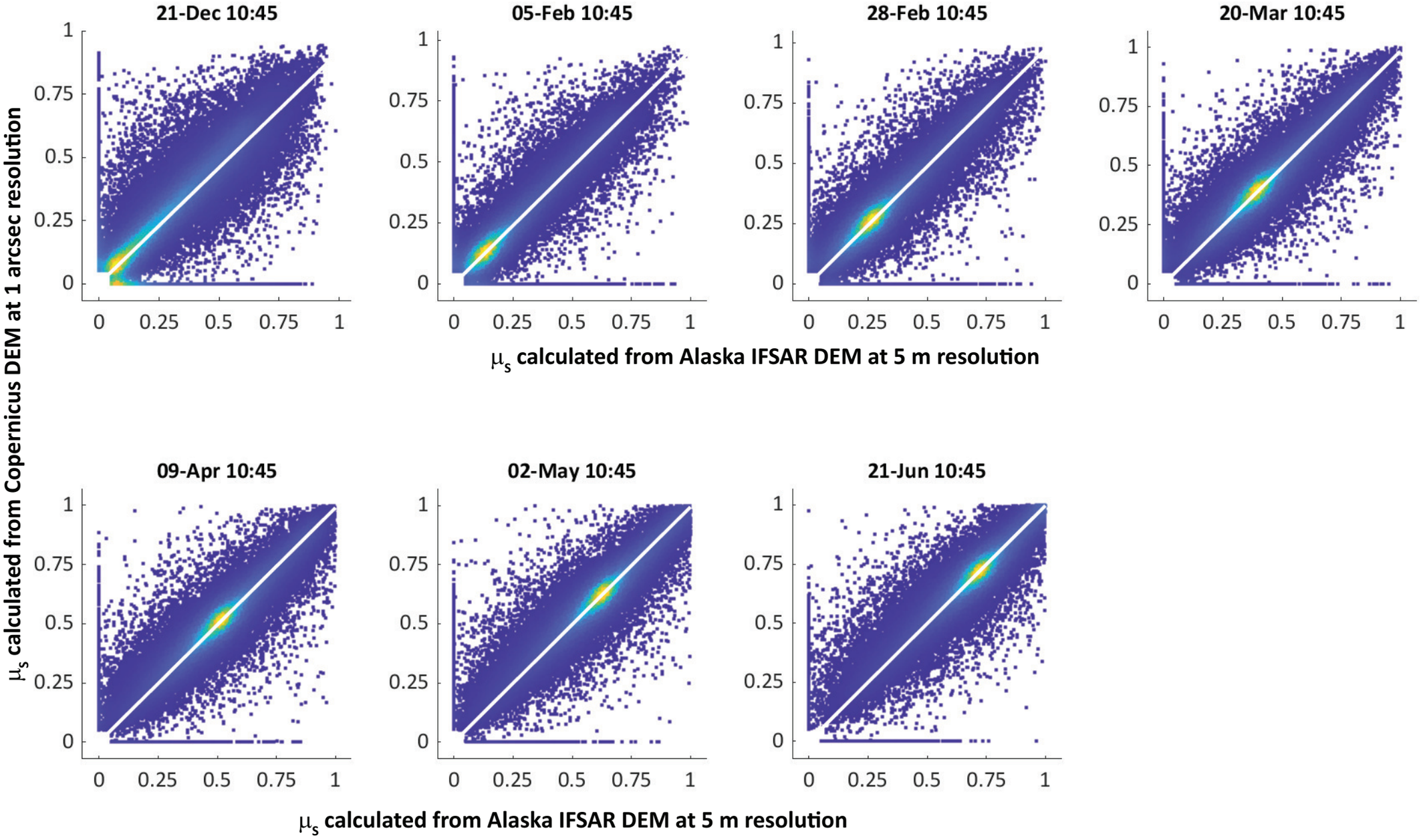
21-Dec 10:45
05-Feb 10:45
28-Feb 10:45
20-Mar 10:45
09-Apr 10:45
02-May 10:45
21-Jun 10:45
μs calculated from Copernicus DEM at 1 arcsec resolution
μs calculated from Alaska IFSAR DEM at 5 m resolution
μs calculated from Alaska IFSAR DEM at 5 m resolution
0
0.25
0.5
0.75
1

Table 1

Dataset	Region	Datum		Elevation		Spatial
		Horizontal	Vertical	Data Source	Projection	resolution
Fine resolution						
ASO DEM	California, Sierra Nevada	WGS84	WGS84	airborne lidar	UTM Zone 11N	3 m
Alaska IFSAR DEM	Alaska, Wrangell Mountains	NAD83	NAVD88	interferometric SAR	Alaska Albers*	5 m
Hign Mountain Asia DEM	Himachal Pradesh, Himalaya	WGS84	WGS84	structure-from-motion	HMA Albers*	8 m
Coarse resolution						
Copernicus DEM	available globally	WGS84	EGM2008	TanDEM-X	geographic	1 arcsec
NASADEM	available globally	WGS84	EGM96	SRTM + ASTER	geographic	1 arcsec

*Albers equaconic projection.

Alaska origin 50°N, 154°W, standard parallels 55°N and 65°N

High Mountain Asia origin 36°N, 85°E, standard parallels 25°N and 47°N

Table 2

RMS Error	elevation (m)	neighbor diff (m)	slope (°)	aspect (°)	view factor
Copernicus DEM, Carson River	4.87	1.86	4.73	36.3	0.0270
NASADEM, Carson River	6.51	2.77	6.24	45.7	0.0339
Copernicus DEM, Himachal Pradesh	15.66	5.72	6.42	26.3	0.0391
NASADEM, Himachal Pradesh	12.06	6.21	6.60	26.7	0.0404
Copernicus DEM, Wrangell Mountains	9.11	3.17	4.15	24.5	0.0248
Bias (%), based on regression slope					
Copernicus DEM, Carson River	0%	-10%	-11%	-2%	-22%
NASADEM, Carson River	0%	-14%	-15%	-3%	-28%
Copernicus DEM, Himachal Pradesh	0%	-5%	-4%	-1%	-5%
NASADEM, Himachal Pradesh	0%	-6%	-6%	-1%	-7%
Copernicus DEM, Wrangell Mountains	0%	-9%	-6%	-1%	-11%
R^2 from regression					
Copernicus DEM, Carson River	1.000	0.832	0.831	0.877	0.782
NASADEM, Carson River	1.000	0.622	0.687	0.798	0.632
Copernicus DEM, Himachal Pradesh	0.999	0.707	0.772	0.933	0.729
NASADEM, Himachal Pradesh	1.000	0.692	0.775	0.931	0.737
Copernicus DEM, Wrangell Mountains	1.000	0.821	0.907	0.954	0.890

Table 3

date		shadowed fraction			μ_s RMS error		μ_s bias, regression based	
(10:45 am)	μ_0	local DEM	Copernicus	NASADEM	Copernicus	NASADEM	Copernicus	NASADEM
ASO DEM, Carson River Watershed								
21-Dec	0.431	9.8%	7.1%	6.6%	0.084	0.105	-2.5%	-3.7%
5-Feb	0.525	4.1%	2.5%	2.5%	0.081	0.101	-1.5%	-2.2%
28-Feb	0.633	1.06%	0.43%	0.54%	0.076	0.094	-0.6%	-0.9%
20-Mar	0.731	0.285%	0.054%	0.099%	0.069	0.085	0.0%	-0.1%
9-Apr	0.815	0.087%	0.004%	0.024%	0.062	0.076	0.4%	0.4%
2-May	0.883	0.023%	0.000%	0.006%	0.054	0.067	0.6%	0.8%
21-Jun	0.925	0.0060%	0.0000%	0.0014%	0.048	0.060	0.8%	1.0%
HMA DEM, Himachal Pradesh, India								
21-Dec	0.495	24%	23%	23%	0.117	0.121	-1.8%	-2.1%
6-Feb	0.575	16%	15%	15%	0.111	0.114	-1.3%	-1.5%
28-Feb	0.668	8.8%	8.2%	8.3%	0.105	0.106	-0.9%	-0.8%
20-Mar	0.757	3.9%	3.4%	3.7%	0.097	0.098	-0.6%	-0.3%
10-Apr	0.835	1.2%	0.9%	1.2%	0.089	0.090	-0.3%	0.1%
3-May	0.891	0.27%	0.18%	0.29%	0.082	0.082	-0.1%	0.4%
21-Jun	0.918	0.083%	0.042%	0.089%	0.078	0.078	0.0%	0.5%
Alaska IFSAR DEM, Wrangell Mountains								
21-Dec	0.028	95%	95%		0.116		-8.2%	
5-Feb	0.143	58%	57%	NASA-	0.072	NASA-	-4.3%	NASA-
28-Feb	0.277	30%	29%	DEM	0.070	DEM	-2.7%	DEM
20-Mar	0.406	16%	16%	extends	0.070	extends	-1.7%	extends
9-Apr	0.527	8.5%	8.0%	only to	0.069	only to	-1.0%	only to
2-May	0.637	3.8%	3.5%	60°N	0.066	60°N	-0.6%	60°N
21-Jun	0.729	1.8%	1.4%		0.063		-0.3%	